Journal of Materials Chemistry B

ROYAL SOCIETY OF CHEMISTRY

PAPER

View Article Online
View Journal | View Issue

Cite this: J. Mater. Chem. B, 2024, 12, 667

Ultrasound-propelled nanomotors for efficient cancer cell ferroptosis†

Ting Chen,[ab] Jie Yang,[a] He Zhao,[a] Dajian Li,[a] Xiaoyong Luo,[a] Zhiyu Fan,[a] Biye Ren, *[b] Yuepeng Cai*[a] and Renfeng Dong *[a]

Received 2nd September 2023,
Accepted 24th November 2023

DOI: 10.1039/d3tb02041j

rsc.li/materials-b

Ferroptosis is a non-apoptotic form of cell death that is dependent on the accumulation of intracellular iron that causes elevation of toxic lipid peroxides. Therefore, it is crucial to improve the levels of intracellular iron and reactive oxygen species (ROS) in a short time. Here, we first propose ultrasound (US)-propelled Janus nanomotors (Au–FeO_x/PEI/ICG, AFPI NMs) to accelerate cellular internalization and induce cancer cell ferroptosis. This nanomotor consists of a gold–iron oxide rod-like Janus nanomotor (Au–FeO_x, AF NMs) and a photoactive indocyanine green (ICG) dye on the surface. It not only exhibits accelerating cellular internalization (~4-fold) caused by its attractive US-driven propulsion but also shows good intracellular motion behavior. In addition, this Janus nanomotor shows excellent intracellular ROS generation performance due to the synergistic effect of the "Fenton or Fenton-like reaction" and the "photochemical reaction". As a result, the killing efficiency of actively moving nanomotors on cancer cells is 88% higher than that of stationary nanomotors. Unlike previous passive strategies, this work is a significant step toward accelerating cellular internalization and inducing cancer-cell ferroptosis in an active way. These novel US-propelled Janus nanomotors with strong propulsion, efficient cellular internalization and excellent ROS generation are suitable as a novel cell biology research tool.

Introduction

Iron is an essential element in the human body, which plays a key role in human health and disease, such as in anemia, diabetes and cancer.[1–3] In particular, cancer cells have a higher demand for iron than normal cells in order to meet their growth requirements, so this dependence on iron makes cancer cells more prone to iron catalyzed necrosis.[4,5] This is a kind of programmed cell death induced by iron-dependent accumulation of lipid peroxidation (LPO) to lethal levels, which is defined as ferroptosis and has attracted extensive attention.[6,7] Studies have shown that iron overload in cancer cells will promote LPO and the accumulation of reactive oxygen species (ROS), resulting in cancer cell ferroptosis.[8,9] Considering the high concentration of hydrogen peroxide (H_2O_2) in the tumor microenvironment (TME), iron-based nanomaterials can induce cell death by catalyzing H_2O_2 to produce ROS in cancer cells.[10–12] However, current iron-based nanoparticles need to be combined with other treatments or require high doses for effective treatments because of their inefficient production of ROS.[13,14] Therefore, how to improve intracellular iron accumulation and intracellular ROS generation to induce more cancer cell ferroptosis is a key issue that needs to be urgently addressed.

Achieving excellent cancer cell ferroptosis involves two important aspects. One key step is to internalize more iron-based nanomaterials into cancer cells leading to more iron accumulation. Another key step is to achieve better catalytic effects to generate more intracellular ROS for cancer cell ferroptosis. Artificial nanomotor is a micro/nano-scale device that can convert external energy into mechanical energy.[15–17] It has many advantages including tiny size, controllable motion, and easy functionalization, thus showing potential for broad applications in many areas, such as environmental governance, biomedicine, and multi-responsive actuators nanofabrication.[18–23] The movement of ultrasound (US)-propelled nanomotors can be controlled using an ultrasonic wireless system.[24,25] This non-contact control method has unique advantages for the practical biological application of nanomotors at the cellular level.[26] In addition, US-propelled nanomotors also have the characteristics of easy functional modification, which can be endowed with specific functions.[27,28] Based on these advantages, US-propelled nanomotors are expected to become a brand-new option for further improving the efficiency of ferroptosis.

Herein, an US-propelled Janus nanomotor (Au–FeO_x/PEI/ICG, AFPI NMs) with rapid propulsion performance was successfully

[a] School of Chemistry, South China Normal University, Guangzhou 510006, China. E-mail: rfdong@m.scnu.edu.cn, caiyp@scnu.edu.cn
[b] School of Materials Science and Engineering, South China University of Technology, Guangzhou 510640, China. E-mail: mcbyren@scut.edu.cn

† Electronic supplementary information (ESI) available. See DOI: https://doi.org/10.1039/d3tb02041j

developed for efficient cancer cell ferroptosis. In this work, the nanomotor consists of a Janus gold–iron oxide nanomotor (Au–FeO_x, AF NMs) and a photoactive indocyanine green (ICG) dye on the surface. ICG is a negatively charged cyanine dye. It can be electrostatically adsorbed on the surface of nanomaterials[29,30] and generate ROS to destroy cancer cells due to its photosensitive properties.[31,32] This nanomotor can be rapidly internalized into cancer cells by US due to the greatly enhanced efficiency of the contact of nanomotors and cells, which improves the cell internalization efficiency (~4-fold) and then retains an active propulsion behavior within the cells. Inside the cells, not only can the Au–FeO_x nanorods catalyze the H_2O_2 *via* Fenton or Fenton-like reaction in the TME to generate ROS but also the ICG can generate ROS under the irradiation of an external near infrared (NIR) laser. Compared with endocytosed nanomotors, the killing efficiency of actively moving nanomotors onto cancer cells has increased by 88%. This autonomous propulsion of nanomotors using US with synergistic functions has broad application prospects in cell biology research.

Results and discussion

Synthesis and characterization

The functional AFPI NMs were prepared using a template-directed electrodeposition method and their surface was modified with ICG *via* electrostatically self-assembling as shown in Fig. 1. The AFPI NMs can rapidly enter the cell under the US field to achieve NIR and TME-responsive cancer cell ferroptosis. The physicochemical properties of AFPI NMs were characterized using various perspectives. The ethylene imine polymer (PEI) and ICG was modified on the Janus nanomotor surface, which was mainly attributed to the electrostatic attraction of opposite charges (Fig. 2A). As shown in Fig. S1 (ESI†), the surface charge of FeO_x carries a positive potential while the surface charge of Au carries a negative potential. Thus, the PEI is difficult to fix on the surface of FeO_x, resulting in ICG being modified on the Au surface *via* electrostatic self-assembly. Scanning electron microscopy (SEM) images were obtained to observe the structural morphology of the AFPI NMs. Fig. 2B shows the motors have a length of 2.4 μm and a diameter of 0.26 μm. Energy dispersive spectroscopy (EDS) displays an obvious distribution of Au, Fe, O, S, C and N along the nanorods. The results of linear scanning distribution of elements on nanomotors in accordance with EDS, indicate the Janus nanomotor was successfully synthesized (Fig. S2, ESI†). The Vis-NIR spectra showed a broad optical absorbance of AFPI NMs at 600 ~ 900 nm (Fig. 2C), suggesting the ICG was successfully modified on the AF NMs. The redshifted broad absorbance peaks could be due to the formation of ICG dimers or oligomers, also known as J-aggregates.[33] In particular, the color of the AF NMs and AFPI NMs aqueous solution was light reddish brown and green, respectively, which further proves the ICG was successfully modified on AF NMs.

Furthermore, the combination of ICG and AF NMs was confirmed by using dynamic light scattering (DLS) measurements. As indicated by the zeta potential of the intermediate and final products shown in Fig. 2D, the change in surface

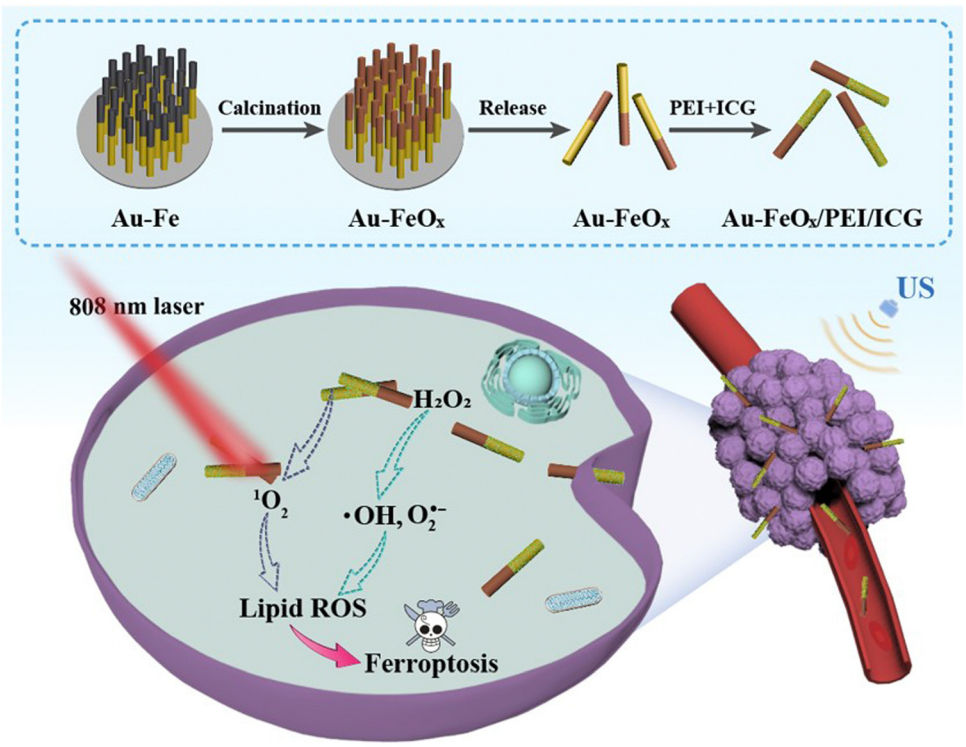

Fig. 1 Schematic illustration of the preparation of AFPI NMs and their induced cancer-cell ferroptosis.

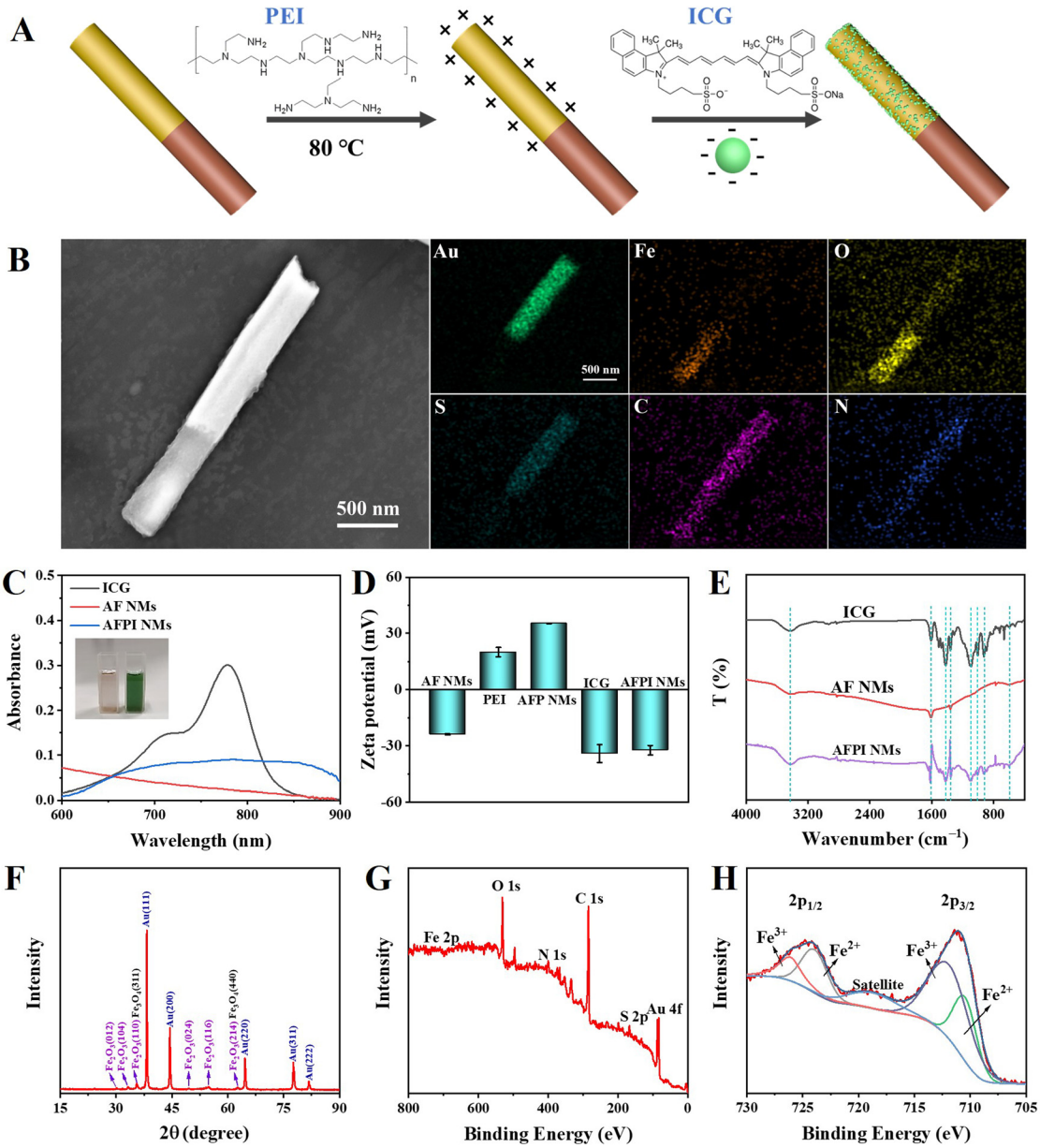

Fig. 2 (A) Schematic of the electrostatic self-assembly for AFPI NMs synthesis. (B) The SEM image of AFPI NMs and the corresponding EDS mapping images for Au, Fe, O, S, C and N, respectively. (C) UV-Vis-NIR absorption spectra of ICG, AF NMs, and AFPI NMs dispersed in water. Inset: The photographs of AF NMs (left) and AFPI NMs (right) dispersed in water. (D) Zeta potentials of the intermediate and final products. (E) FT-IR spectra of ICG, AF NMs and AFPI NMs. (F) XRD pattern of AFPI NMs. XPS spectra of the (G) survey spectrum and (H) Fe 2p peaks in AFPI NMs.

potential from negative to positive to negative demonstrated the successful assembly of positively charged PEI and negatively charged ICG on AF NMs through electrostatic interaction. To confirm the ICG molecules were adsorbed onto AF NMs, the Fourier transform infrared (FT-IR) spectroscopy of the prepared AF NMs, AFPI NMs and free ICG were measured (Fig. 2E). The obvious absorption at 3421 cm^{-1} and 1620 cm^{-1} correspond to the O–H stretching, 1354 cm^{-1} is ascribed to the C–N stretching, 603 cm^{-1} is ascribed to the Fe–O vibration, and the typical peaks at 900–1100 cm^{-1} and 1400–1500 cm^{-1} were attributed to the vinyl stretches and C=C stretches, respectively.[33] The FT-IR spectra of the final product contained the above characteristic peaks of AF NMs and ICG, which further confirmed the successful synthesis of AFPI NM composites.

As the X-ray diffraction (XRD) patterns in Fig. 2F show, the AFPI NM segment contained mostly α-Fe_2O_3 (JCPDS number 33-0664). The two most intense reflections of magnetite (Fe_3O_4), the (311) and (440), overlap with the (110) and (214) reflections of hematite (α-Fe_2O_3), respectively, pointing to the possible presence of Fe_3O_4 in the AFPI NM segments. Finally, X-ray photoelectron spectroscopy (XPS) measurements indicated the existence of mixed oxidation states for iron, namely Fe^{2+} and Fe^{3+}, suggesting the presence of a magnetite (Fe_3O_4) phase (Fig. 2G and H). Furthermore, based on the proportion of Fe^{2+} and Fe^{3+}, the percentage of

x in FeO_x is 1.37 (x = 1.37 in AFPI NMs). Besides, two peaks of Au 4f were located at 83.7 and 87.3 eV, which correspond to Au^0 $4f_{7/2}$ and Au^0 $4f_{5/2}$, respectively (Fig. S3, ESI†).

Motion performance

In the typical experiment, the oscillation of the nanorod in the direction of the acoustic excitation generates a streaming flow. That flow in turn exerts stresses on the asymmetric nanorod that drive its oscillation in the levitation plane. Because the density of the nanorods is higher than that of the surrounding fluid, their inertia is significant at high driving frequencies. When the nanorod is asymmetric, the streaming effect results in a net force along the axis of the rod, propelling it toward its concave end. Additionally, the recent discovery that rocket-shaped metallic nanorods can be propelled in fluids by acoustic energy in the megahertz (MHz) regime presents some promise for penetrating living cells and actuation within living cells.[34,35]

The AFPI NMs have excellent propulsion performance in solutions under the US field, even after modification with ICG, which is crucial for efficient cell internalization. The propulsion behaviors of AF NMs and AFPI NMs in different solutions were compared under a US field at 15.0 V and 3.7 MHz. As shown in Fig. 3A (taken from Video S1, ESI†), the average speeds of the AFPI NMs were calculated to be 34.1 μm s^{-1} and 32.6 μm s^{-1} in deionized water and DMEM culture

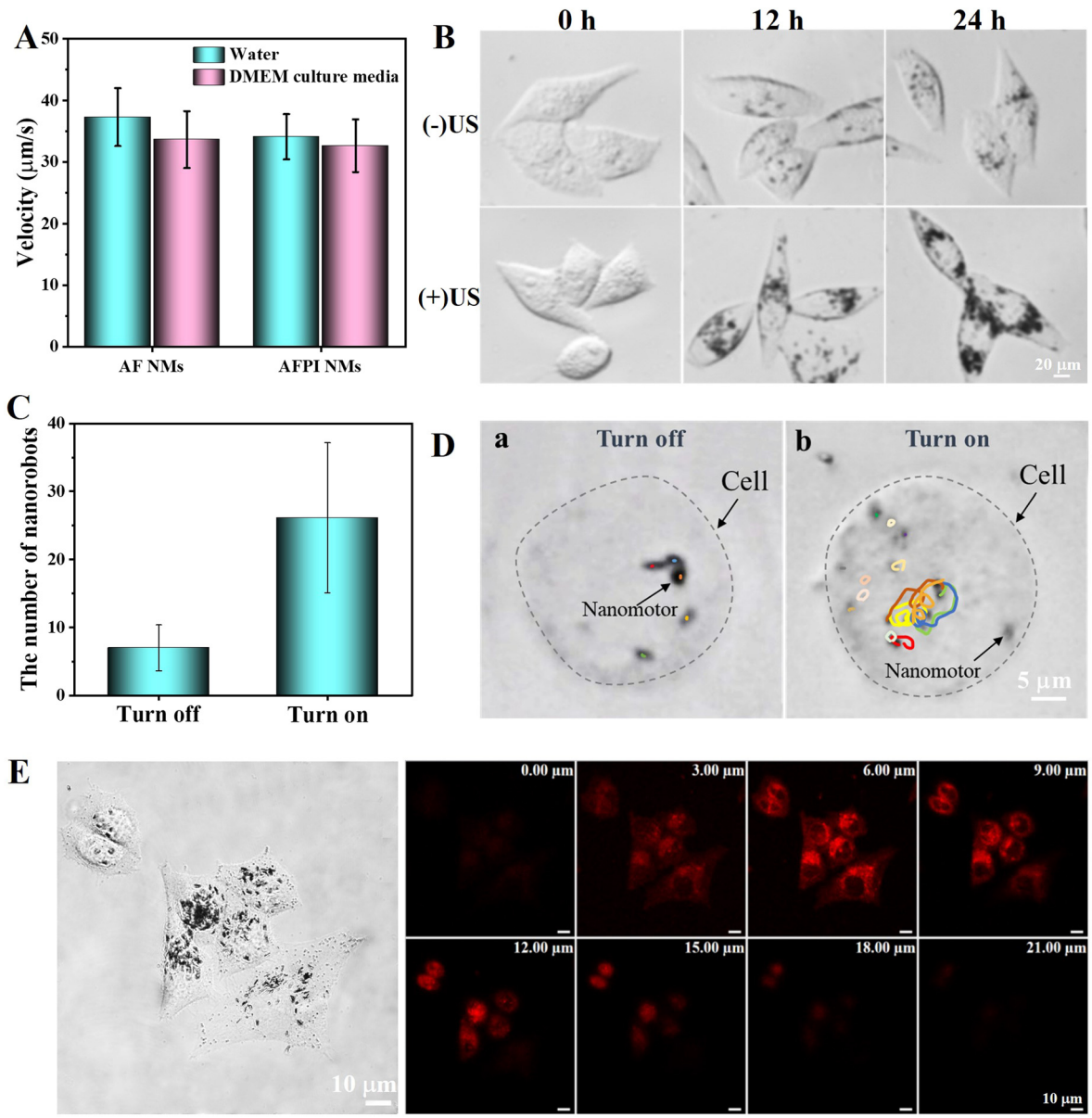

Fig. 3 (A) The average speed of nanomotors under a US field in different solutions. (B) Microscope image of AFPI NMs distribution in MCF-7 cells treated with US on/off and incubation for different times. (C) The number of AFPI NMs entering MCF-7 cells after treating with US on/off. (D) Time-lapse images showing the tracking trajectories of AFPI NMs intracellularly, taken from Video S3 (ESI†) within 3 s of treating with US on/off. (E) Z-stacked scanning CLSM image of MCF-7 cells cultured with AFPI NMs under an US field and incubation for 12 h. The scanned height was 21 μm and the z spacing was 3 μm.

medium, respectively. The average speeds of the AF NMs were 37.2 μm s^{-1} and 33.6 μm s^{-1}, respectively (taken from Video S2, ESI†). This result indicates that nanomotors can also exhibit excellent propulsion capabilities in high-viscosity solutions (DMEM culture medium). Despite this small change of propulsion in the nanomotors, the motion of the AFPI NMs provided sufficient thrust for cell contact and subsequent intracellular propulsion.

Cellular internalization

Considering that the cancer cells and tissues produce large amounts of H_2O_2, the MCF-7 cells was selected as a cancer cell model for exploring the internalization efficiency and cancer cell-killing effect of nanomotors in this work.[36] Under specific US conditions, the probability of contact between nanomotors and cells increases, and the nanomotors can quickly approach cells, leading to rapid cellular internalization.[27] The MCF-7 cells were treated for 5 min with the AFPI NMs under the US on/off and then cultured for different times (0 h, 12 h, 24 h) to observe the cellular internalization using a microscope. As illustrated by the microscope images in Fig. 3B and C, compared to the control group treated with the US off, it can be observed that more AFPI NMs enter the MCF-7 cell with the aid

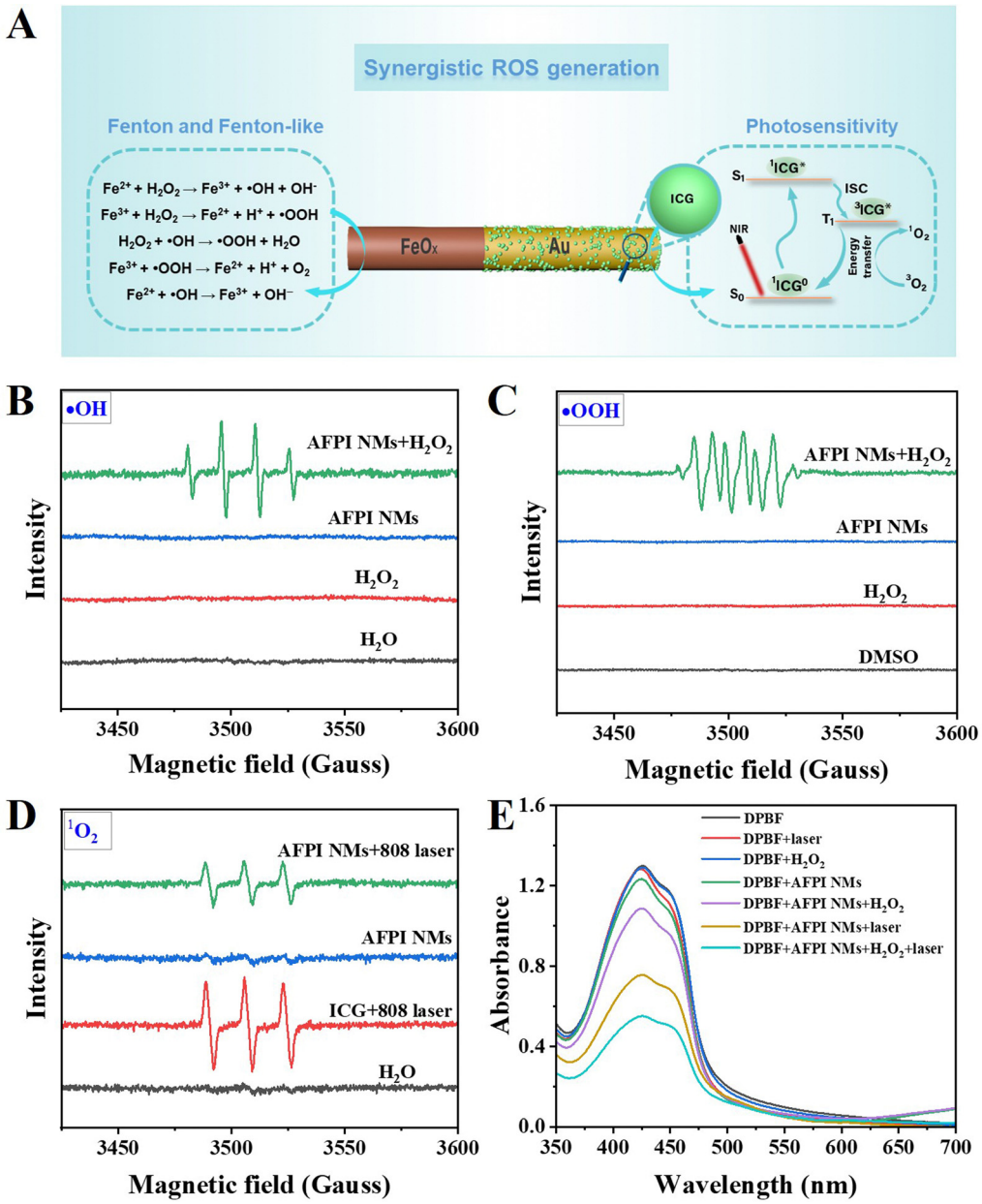

Fig. 4 (A) Mechanism of H_2O_2 catalyzed by AFPI NMs and $^1O_2$ generation from excited ICG in AFPI NMs induced by NIR irradiation. S_0, singlet ground state; S_1, the lowest singlet excited state; ISC, intersystem crossing; T_1, the lowest triplet excited state. EPR spectra of AFPI NMs trapped by DMPO to detect the (B) •OH signal in MeOH, and (C) •OOH signal in DMSO in the presence of 0.5 mM H_2O_2, respectively. (D) EPR spectra of AFPI NMs trapped by TEMP to detect the $^1O_2$ signal in H_2O under an 808 nm laser. (E) UV–Vis spectra of DPBF after treating with different formulations.

of US and without destroying the integrity of the cell due to its excellent active propulsion performance in the US field. The average number of AFPI NMs entering cells was calculated to be 7 and 27 with the US off and the US on at 12 h, respectively. This result proves that the US can dramatically improve the number of nanomotors entering the cells (~4-fold). Additionally, although internalized AFPI NMs are hindered by intracellular barriers, the internalized AFPI NMs remained acoustically active after entering the MCF-7 cells and performed motions actively inside the cells as shown in Fig. 3D and Video S3 (ESI†).

Furthermore, the ability of AFPI NMs to enter cells was confirmed using a confocal laser scanning microscope (CLSM), which is crucial for achieving ferroptosis. A 3D surface projection of Z-stack images was used to visualize the distribution of intracellular ICG. As shown in the Z-stack scan CLSM images in Fig. 3E and Fig. S4 (ESI†), as expected, the red fluorescence of ICG was distributed intracellularly and showed a trend of first increasing and then decreasing with increasing scan height, implying that AFPI NMs were successfully internalized into cells.

ROS detection

The AFPI NMs can generate multiple ROS under the H_2O_2 and NIR laser (808 nm) irradiation, which plays a vital role in cellular LPO. These multiple ROS include singlet oxygen ($^1O_2$), hydroxyl radical ($^\bullet$OH), and hydroperoxyl radicals ($^\bullet$OOH). Based on the previous studies, the possible mechanism of ROS generation is proposed in Fig. 4A. On the FeO_x surface, the H_2O_2 activation may be induced by Fe^{2+} and Fe^{3+} species according to previous studies.[37] The oxidation process between H_2O_2 and Fe^{2+} begins with the Fenton reaction that allows the generation of $^\bullet$OH. Then, the formed Fe^{3+} and $^\bullet$OH can further react with H_2O_2 to produce $^\bullet$OOH. Lastly, the formed $^\bullet$OOH and $^\bullet$OH react with Fe^{3+} and Fe^{2+} producing other species, separately (Fig. 4A). On the Au surface, the mechanism of ICG generating ROS might be explained by the following process: the electrons in the ICG transferred from the ground state (S_0) to the first excited state (S_1), and then the energy was transferred to the lowest triplet excited state (T_1) through the intersystem crossing (ISC); thus, the surrounding O_2 molecules were transformed into $^1O_2$ *via* an energy-transfer process. The generation of multiple ROS ($^\bullet$OH, $^\bullet$OOH and $^1O_2$) by AFPI NMs was verified using electron paramagnetic resonance (EPR) spectroscopy. The EPR signals of AFPI NMs were recorded using 2,2,6,6-tetramethylpiperidine (TEMP) as the $^1O_2$ trapper, and 5,5-dimethyl- 1-pyrroline *N*-oxide (DMPO) as the $^\bullet$OH and $^\bullet$OOH trapper.[38] As shown in Fig. 4B, a characteristic signal of DMPO-$^\bullet$OH adduct was recorded in the presence of H_2O_2, proving the formation of $^\bullet$OH. To prove whether $^\bullet$OH is

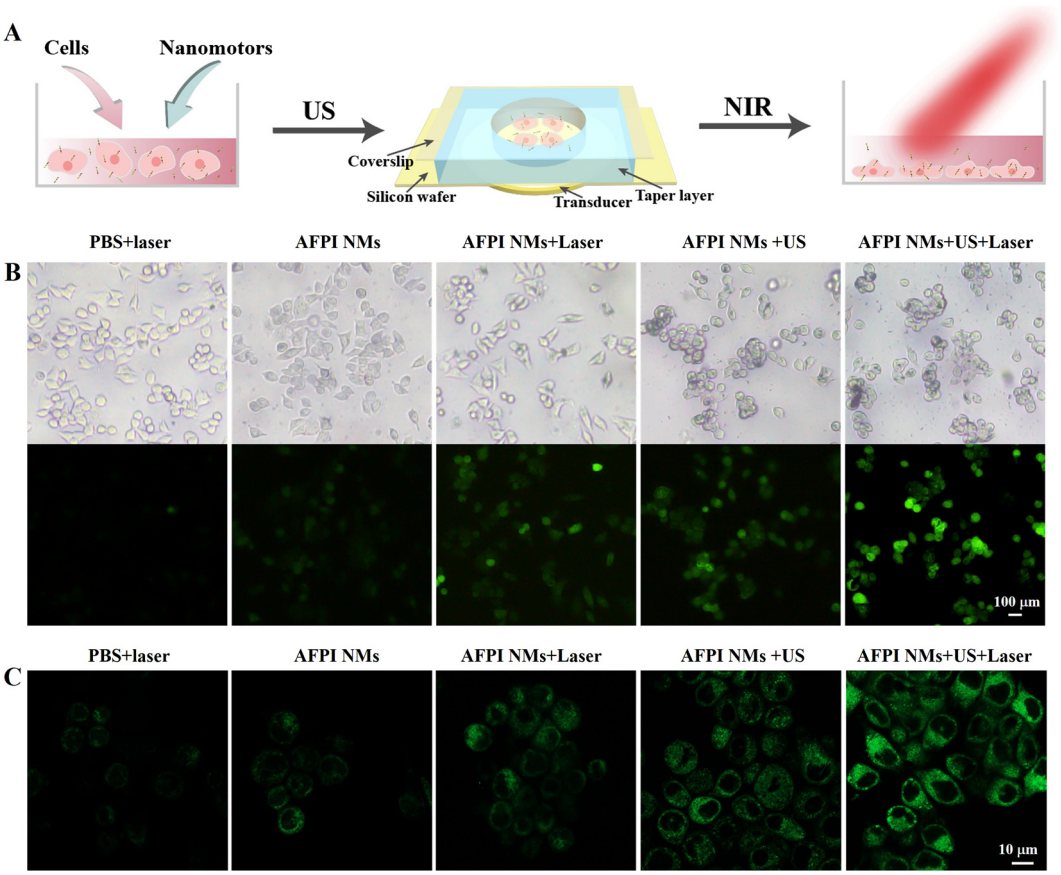

Fig. 5 (A) Schematic diagram of the ultrasound and laser irradiation process. (B) Fluorescence images of ROS generation in MCF-7 cells detected by using DCFH-DA. (C) Fluorescence images of LPO in MCF-7 cells detected by using BODIPY$^{581/591}$-C11.

the sole ROS, we also evaluated the formation of •OOH. In the presence of H_2O_2, a characteristic signal of adduct of •OOH with DMPO (DMPO-OOH) was detected when dimethyl sulfoxide (DMSO) was used as the solvent (Fig. 4C), because •OOH is unstable in water solution.[39] Furthermore, the TEMP-$^1O_2$ adduct (Fig. 4D) was also recorded under the laser (808 nm, 2 W cm^{-2}, 5 min irradiation) in the presence of AFPI NMs or ICG. Finally, to examine the capacity of AFPI NMs for synergetic generation of ROS induced by H_2O_2 and laser irradiation, the 1,3-diphenylbenzofuran (DPBF) chemical trapping method was used. The ROS (*e.g.*, $^1O_2$, •OH and •OOH) can oxidize DPBF, which leads to a decrease in the UV–Vis absorption. As shown in Fig. 4E and Fig. S5 (ESI†), the absorption of DPBF at 425 nm decreased by 16.4% after 5 min of incubation in the presence of AFPI NMs and H_2O_2. When the AFPI NM solution was only irradiated for 5 min, it was decreased by 41.7%, indicating that either H_2O_2 or 808 nm laser irradiation could induce AFPI NMs to generate ROS. Additionally, it was found that the absorption decreased by 57.5% after being treated with H_2O_2 and 808 nm laser irradiation for 5 min. These results confirm that irradiation by the 808 nm laser and H_2O_2 is essential for the synergetic generation of ROS.

These results indicated that multiple ROS can be generated, which all contribute to achieving LPO. Here, the schematic diagram of the US and laser irradiation process is shown in Fig. 5A. The 2,7-dichlorofluorescein diacetate (DCFH-DA) was used to determine the ROS generation in MCF-7 cells due to the ability to emit green fluorescence after being oxidized by ROS.[40] After treatment with AFPI NMs under the laser or US, the MCF-7 cells displayed green fluorescence, in marked contrast to the lack of fluorescence signal in the groups treated with only PBS + laser or AFPI NMs (Fig. 5B). When the cells were co-incubated with AFPI NMs and a laser under the US, a stronger green fluorescence appeared, indicating that the US and laser can synergistically generate ROS in intracellular environments. BODIPY$^{581/591}$-C11 is an LPO sensor used to detect LPO generation by microscopy. As shown in Fig. 5C, the MCF-7 cells treated with the AFPI NMs + US + laser exhibited stronger green fluorescence (representing more LPO) in the cell membrane than the cells treated with PBS + laser or strictly AFPI NMs, implying the significant contribution of the US and laser to enhance ferroptosis. These results indicate that AFPI NMs can effectively generate intracellular ROS under the US and laser, which has the potential to further achieve cancer cell ferroptosis.

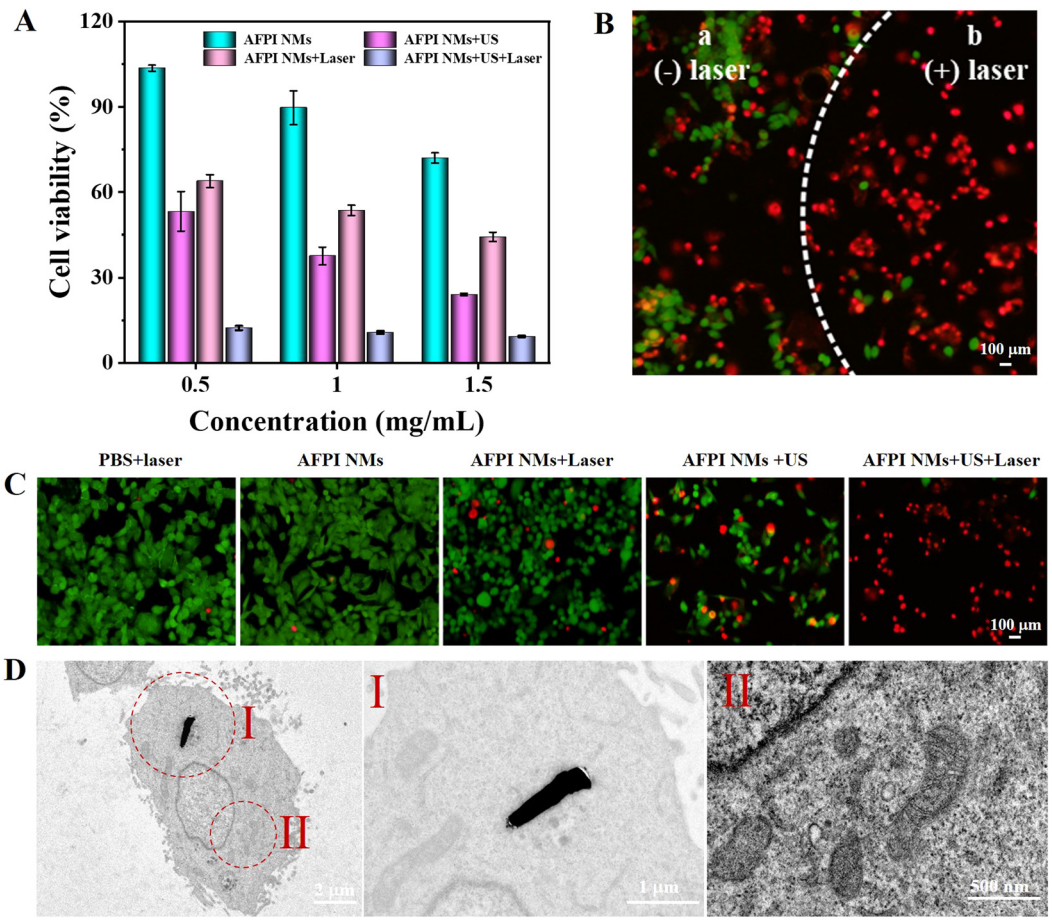

Fig. 6 (A) Viability of MCF-7 cells treated with different methods for 24 h. Fluorescence images of the live-dead staining in MCF-7 cells incubated with AFPI NMs, (B) under an US field and exposure to 808 nm laser irradiation (2 W cm^{-2}) for 5 min, and (C) treated with different methods. (D) Bio-TEM image of the cross-section of MCF-7 cell and its local view (I, II) after being incubated with AFPI NMs for 12 h.

Synergistic properties

Studies have shown that iron overload and the accumulation of ROS in cancer cells may promote LPO, resulting in cancer cell ferroptosis.[8,9] Here, the standard Cell Counting Kit-8 (CCK-8) assay was used to evaluate the ability of killing MCF-7 cells. Firstly, the cytotoxicity of cells under separate US and laser stimulation conditions were both explored. As shown in Fig. S6 (ESI†), the cell viability is greater than 97% in all cases, showing the negligible cytotoxicity of US and laser irradiation and both together toward MCF-7 cells. These results guarantee their suitability for further synergistic-induced cancer cell ferroptosis investigation. As shown in Fig. 6A, within the range of AFPI NM concentration of 0.5 ~ 1.5 mg mL^{-1}, the cell viability of MCF-7 cells gradually decreased after incubation for 24 h. In particular, when the AFPI NM concentration was 0.5 mg mL^{-1}, cell viability was reduced to 53% after cells were treated with US, indicating that the active propulsion of nanomotors induced by US can accelerate cellular internalization to lead to a better cell-killing effect. Under US + laser irradiation, the cell viability was only about 12%. Compared with US (53%) and laser irradiation (64%) alone, the synergistic effect can substantially enhance intracellular ROS generation to achieve a more effective cancer cell-killing effect. Normal human liver cells (HL-7702) were further used as a control to explore the effects of different modalities of treatment on HL-7702 cells with low H_2O_2 expression. Fig. S7 (ESI†) implies that the cell viability treated with US and US + laser irradiation was higher than that of MCF-7 cells due to the low H_2O_2 concentration in HL-7702 cells leading to low ROS generated. This result proves that the AFPI NMs can effectively create synergism inducing cancer cell ferroptosis in high H_2O_2 expression cells. Then, the cytotoxicity of AFPI NMs toward MCF-7 cells was further determined by visual evidence of cell survival from a live-dead cell staining assay, where calcein-AM and propidium iodide (PI) were used to identify living cells and dead cells, respectively.[41] As shown in Fig. S8 (ESI†), a strong green fluorescence signal and negligible red fluorescence signal were observed in the PBS, US, laser and US + laser groups, indicating that MCF-7 cells could not be destroyed with US, laser irradiation and both of them. The efficiency of AFPI NMs under the US or laser irradiation induced the destruction of more MCF-7 cells, giving rise to a large area of red fluorescence compared to those only treated with AFPI NMs. Notably, the efficiency of AFPI NMs combined with US or laser irradiation caused almost all cells to die, as indicated by the intense homogeneous red fluorescence (Fig. 6B and C). CCK-8 assay and live-dead cell staining assay confirmed that the combined US and laser irradiation dual-modality function based on AFPI NMs constituted a more efficient therapeutic protocol against cancer cells than either US or laser irradiation alone. Additionally, the morphological changes in the cell's mitochondria after treatment with AFPI NMs under US and laser irradiation were monitored to evaluate the effect of ferroptosis. As shown in Fig. 6D, the mitochondria in AFPI NM-treated cells were observed to shrink, which is consistent with previous results of ferroptosis. These results demonstrate that AFPI NMs can induce cell ferroptosis under US and laser irradiation.

Conclusion

In conclusion, we confirmed that the US-propelled Janus nanomotor prepared *via* the template electrodeposition method exhibited excellent functionality for inducing cancer cell ferroptosis. Owing to the acoustic waves, these US-propelled nanomotors show rapidly propulsion toward cancer cells and maintain acoustic activity within cells. Intracellularly, iron oxide can produce ROS by catalyzing H_2O_2 *via* Fenton or Fenton-like reaction in the TME. In addition, the ICG that was modified on the surface of nanomotors can also produce ROS under NIR irradiation. The synergistic ROS produced by these two mechanisms can induce LPO of cells, resulting in effective cancer cell ferroptosis (cell viability rate as low as 12%). This work combines the motion characteristics and the advantages of synergistic ROS generation of multifunctional nanomotors, which not only enhance cellular uptake but can also easily achieve their functional applications, show great potential for drug delivery and are suitable as a tool for cell biology research such as cell death.

Experiments

Materials

Alumina membrane templates (AAO, 100 nm pore size) were purchased from Whatman (cat. No. 110407). Silver-plating electroplate liquid (Orotemp 24 RTU RACK and 1025 RTU at 4.5 Troy/gallon) was purchased from Technic Inc. (Anaheim, CA). Boric acid (H_3BO_3), ascorbic acid ($C_6H_8O_6$), iron sulfate heptahydrate ($FeSO_4{\cdot}7H_2O$), glutaraldehyde (50% in H_2O), 4-amino-2,2,6,6-tetramethylpiperidine (TEMP), and 5,5-dimethyl-1-pyrroline *N*-oxide (DMPO) were purchased from Aladdin Bio-Chem Technology Co., Ltd. Sulfamic acid (H_3NO_3S), ethylene imine polymer (PEI, M.W. 70000), indocyanine green (ICG, $C_{43}H_{47}N_2NaO_6S_2$), potassium bromide (KBr), and 1,3-diphenylisobenzofuran (DPBF) were purchased from Macklin Biochemical Technology Co., Ltd. Hydrogen peroxide (H_2O_2) was purchased from Alfa Aesar (A Johnson Matthey Company). 2′,7′-Dichlorodihydrofluorescein diacetate (DCFH-DA), calcein-AM, and propidium iodide (PI) were purchased from Beyotime Biotechnology Co., Ltd (Shanghai). Cell Counting Kit-8 (CCK-8) was purchased from ApexBio Technology. Dulbecco's Modified Eagle Medium (DMEM) and fetal bovine serum (FBS) were purchased from Thermo Fisher Technology Co., Ltd. Phosphate buffered saline (PBS) and trypsin were purchased from Jiangsu KeyGEN Bio TECH CoRP., Ltd. C11-BODIPY$^{581/591}$ was purchased from GlpBio Technology. All commercially purchased reagents and solvents were used without further purification unless specifically noted. Ultrapure Milli-Q water (18.2 MW) was used in all experiments.

Nanomotor preparation and modification

The gold–iron oxide nanomotors (Au–FeO_x, AF NMs) were synthesized according to the template-directed electrodeposition method.[42] AAO (100 nm pore size) was used as the template for the electrodeposition of AF NMs. Firstly, a thin

layer of Ag was sputtered on the porous AAO film. Then, the sacrificial Ag segment was electrodeposited for 15 min into the AAO film at a current of −1.6 mA cm^{-2}. Then, gold was deposited for 30 min at a current density of 0.8 V (*vs.* Ag/AgCl). Afterward, Fe was electrodeposited for 60 min at a current density of 0.85 V (*vs.* Ag/AgCl). Au plating solution was self-prepared. Fe plating solution was prepared by mixing 0.6 g of iron sulfate heptahydrate, 0.015 g of ascorbic acid, 0.005 g of sulfonic acid and 0.15 g of boric acid in 10 mL of ultra-pure water. After electrodeposition, the Ag layer was removed using 8 M HNO_3 solution and then the AAO membrane with gold–iron nanorods was thermally annealed under an oxygen atmosphere for 10 h at 500 °C to convert iron into iron oxide. Finally, the AAO membrane was removed with 3 M NaOH solution for 0.5 h and rinsed with ultra-pure water three times.

In order to obtain a better cell-killing effect, ICG was modified on the surface of AF NMs *via* electrostatic interaction. Cationic PEI was assembled on the negatively charged AF NMs by electrostatic interaction to form Au–FeO_x/PEI nanomotors (AFP NMs). Briefly, PEI solution (10 mL, 20 mg mL^{-1}, pH = 5) was slowly introduced into the AF NMs dispersion (10 mL) under stirring at 80 °C. After 30 min, the products were purified and collected by centrifugation. Subsequently, negatively charged ICG was adsorbed onto positively charged AFP NMs based on electrostatic interaction. To avoid ICG degradation, this step synthetic procedure was accomplished in the dark. Typically, ICG solution (1 mg mL^{-1}, 10 mL) was added dropwise into an AFP NM dispersion (20 mL). After 12 h of mixing, AFPI NMs were purified and collected by centrifugation with ultra-pure water three times.

Nanomotors' motion calibration

The steps for calibrating the velocity of US-propelled nanomotors are as follows: 10 μL of AF NMs or AFPI NMs dispersed in water or DMEM culture medium were dropped onto the acoustic cell dish to track the motion state using an inverted optical microscope (Nikon Instruments Inc. Ti-S/L100) in dynamic state under the US field (15 V, 3.7 MHz). Videos were captured using a Hamamatsu ORCAflash 4.0 LT (C11440) sCMOS digital camera coupled with 40× objectives. For each condition, 50 nanomotors were randomly selected for velocity analysis. The trajectories and the velocities of the nanomotors were tracked using the NISElements AR 4.3 software.

ROS detection

DPBF is a molecule that possesses a highly specific reactivity toward ROS. This reaction between DPBF and ROS can be followed by measuring the decrease in absorbance intensity of DPBF with a Shimadzu UV-Vis-NIR spectrophotometer UV-2700. The detailed procedure is as follows:

Detection of ROS in Fenton and Fenton-like reaction: 20 μL DPBF (1 mg mL^{-1}), 10 μL H_2O_2 (200 mM), 10 μL AFPI NMs (10 mg mL^{-1}), and 1960 μL PBS buffer solutions were combined to make the final reaction volume of 2 mL. Then, the mixed solution obtained in the previous step was left to stand for 5 min. Finally, the solution was transferred into a quartz cell and its UV absorption at 350–700 nm was measured using a spectrophotometer UV-2700.

Detection of ROS in the photosensitivity reaction: 20 μL DPBF (1 mg mL^{-1}), 10 μL AFPI NMs (10 mg mL^{-1}), and 1970 μL PBS buffer solutions were combined to make the final reaction volume of 2 mL. Then, the mixed solution obtained in the previous step was irradiated with an 808 nm laser for 5 min. Finally, the solution was transferred into a quartz cell and its UV absorption at 350–700 nm was measured with a spectrophotometer UV-2700.

Detection of synergistic ROS generation: 20 μL DPBF (1 mg mL^{-1}), 10 μL H_2O_2 (200 mM), 10 μL AFPI NMs (10 mg mL^{-1}), and 1960 μL PBS buffer solutions were combined to make the final reaction volume of 2 mL. Then, the mixed solution obtained in the previous step was irradiated with an 808 nm laser for 5 min. Finally, the solution was transferred into a quartz cell and its UV absorption at 350–700 nm was measured using a spectrophotometer UV-2700.

Similarly, other control group experiments were conducted using similar methods.

EPR measurement

DMPO was used as a spin-trapping reagent to detect $^{\bullet}OH$ and $^{\bullet}OOH$ generation by EPR. First, AFPI NMs (10 μL, 10 mg mL^{-1}), PBS (70 μL, pH = 7.0), H_2O_2 (10 μL, 1 mM), and DMPO (10 μL, 0.8 M) were mixed to prepare the test solution. Then, the processed solution was placed in the EPR chamber for testing. In addition, TEMP was used as a spin-trapping reagent to detect $^1O_2$ generation by EPR with a similar method. First, AFPI NMs (10 μL, 10 mg mL^{-1}), PBS (80 μL, pH = 7.0), and TEMP (10 μL, 0.8 M) were mixed and then irradiated with an 808 nm laser for 5 min. Finally, the processed solution was placed in the EPR chamber for testing. Similarly, other control group experiments were conducted using similar methods.

Cell viability

The biocompatibility of nanomotors was evaluated *via* the CCK-8 assay. MCF-7 cells (10 μL, containing 1×10^4 cells) and different concentrations of 5 μL AFPI NMs (1.5, 3, 4.5 mg mL^{-1}) were mixed then incubated for 4 h. Then, the cells were transferred into a specialized US dish and the US was turned on for 5 min (15 V, 3.7 MHz). Next, the cells were transferred into a 96-well plate containing 85 μL DMEM culture medium, and incubated in the cell incubator (37 °C, 5% CO_2) for 24 h. Subsequently, the liquid in the dish was removed and washed 3 times with PBS, and irradiated with an 808 nm laser for 5 min. Finally, the liquid in the dish was removed, 90 μL DMEM culture medium and 10 μL of CCK-8 solution were added to each well. The samples were incubated in the incubator for 1 h, and the absorbance of the 96-well plate at 450 nm was recorded using a microplate reader. Similarly, the cell viability effect induced by the photosensitivity reaction or Fenton/Fenton-like reaction was also evaluated using the same method. The value measured by absorbance at 450 nm was directly proportional to the number of living cells. The percentage of viability was

calculated assuming that the average absorbance of the wells containing non-treated cells represented 100% viability.

Intracellular ROS detection

Intracellular ROS generation was detected by using DCFH-DA. MCF-7 cells and AFPI NMs (0.5 mg mL^{-1}) were co-incubated in the chamber at 37 °C for 4 h. Then, the cells were transferred into a specialized US dish and the US was turned on for 5 min (15 V, 3.7 MHz). The cells were transferred into a 24-well plate containing 500 μL DMEM culture medium, and incubated in the cell incubator (37 °C, 5% CO_2) for 12 h. Next, the cells were washed three times with PBS buffer solution to remove extracellular nanomotors and irradiated with an 808 nm laser for 5 min. Subsequently, they were incubated with DCFH-DA (10 mM) for 20 min in the dark, and DCFH-DA was loaded into the cells. Finally, the fluorescence images of treated cells were acquired using an orthostatic optical microscope (OLYMPUS, DP74). Similarly, other control group experiments were conducted using similar methods.

Intracellular LPO generation

$BODIPY^{581/591}$-C11 was used to assess the intracellular LPO level. This is a fluorescent probe for LPO detection that can be inserted into lipid membranes and oxidized by intracellular LPO. The oxidized products display green fluorescence. MCF-7 cells and AFPI NMs (0.5 mg mL^{-1}) were co-incubated in the chamber at 37 °C for 4 h. Then, the cells were transferred into a specialized US dish and the US was turned on for 5 min (15 V, 3.7 MHz). The cells were transferred into a 24-well plate containing 500 μL DMEM culture medium, and incubated in a cell incubator (37 °C, 5% CO_2) for 12 h to allow the cells to attach to the surface of the wells. After incubation for 12 h, the cells were washed twice with PBS buffer solution to remove extracellular nanomotors, and irradiated with an 808 nm laser for 5 min. Subsequently, after incubating with $BODIPY^{581/591}$-C11 (50 μM) for 30 min in the dark, the cell membranes were stained with $BODIPY^{581/591}$-C11. Finally, fluorescence images of the treated cells were acquired using laser confocal scanning microscopy (LSM880 NLO, Zeiss). Similarly, other control group experiments were conducted using similar methods.

Live-dead cytotoxicity assay

The cytotoxicity of MCF-7 cells was evaluated using live-dead staining assay in which calcein-AM was used to visualize the live cells and PI to visualize the dead cells. Calcein-AM can permeate into the cell membrane and be hydrolyzed by intracellular esterases into a green fluorescent dye of calcein in living cells, whereas the cell nucleus dye of PI can only cross damaged cell membranes and embed into double-stranded DNA to show red fluorescence in dead cells. Thus, based on the above characteristics, calcein-AM and PI are used to label living and dead cells, respectively. Briefly, MCF-7 cells and AFPI NMs (0.5 mg mL^{-1}) were co-incubated in the chamber at 37 °C for 4 h. Then, the MCF-7 cells were treated with different methods and transferred to a 24-well plate containing 500 μL DMEM culture medium, and incubated in a cell incubator (37 °C, 5% CO_2) for 12 h. After that, PBS buffer solution was used to wash the cells three times to remove the extracellular nanomotors. Subsequently, 1.6% calcein-AM and 2% PI were used to stain the cells for 5 min and 7 min, respectively. Finally, the fluorescence images were recorded using an orthostatic optical microscope (OLYMPUS, DP74).

Cellular TEM imaging

MCF-7 cells were treated with AFPI NMs (0.5 mg mL^{-1}) under an US field (15 V, 3.7 MHz) for 5 min. After incubation for 12 h, the cells were irradiated using a NIR laser (2 W cm^{-2}). Then, the cells were washed with PBS three times and the collected cells were fixed with 2.5% glutaraldehyde. Lastly, the overall morphology and ultrastructure changes of the cells were observed under an electron microscope (JEM-1200EX).

Author contributions

Ting Chen: conceptualization, methodology, data curation, writing – original draft. Jie Yang: data curation, formal analysis, visualization. He Zhao: data curation, formal analysis. Dajian Li: writing – review & editing. Zhiyu Fan: visualization, investigation. Xiaoyong Luo: validation. Biye Ren: supervision. Yuepeng Cai: supervision. Renfeng Dong: writing – reviewing and editing, providing funding.

Conflicts of interest

There are no conflicts to declare.

Acknowledgements

This work was supported by the General Project of Natural Science Foundation of Guangdong Province (2022A1515010715), the Science and Technology Planning Project of Guangdong Province (2017B090917002, 2019B1515120027 and 2019A050510038), and Research and development plan projects in key areas of Guangdong Province (2020B0101030005).

References

1 M. Nairz and G. Weiss, *Mol. Aspects Med.*, 2020, **75**, 100906.
2 N. K. Das, A. J. Schwartz, G. Barthel, N. Inohara, Q. Liu, A. Sankar, D. R. Hill, X. Ma, O. Lamberg, M. K. Schnizlein, J. L. Arques, J. R. Spence, G. Nunez, A. D. Patterson, D. Sun, V. B. Young and Y. M. Shah, *Cell Metab.*, 2020, **31**, 115–130 e116.
3 V. Cejvanovic, L. K. Kjaer, H. K. Morup Bergholdt, T. Henriksen, A. Weimann, C. Ellervik and H. E. Poulsen, *Free Radical Biol. Med.*, 2018, **129**, 532–536.
4 V. Trujillo-Alonso, E. C. Pratt, H. Zong, A. Lara-Martinez, C. Kaittanis, M. O. Rabie, V. Longo, M. W. Becker, G. J. Roboz, J. Grimm and M. L. Guzman, *Nat. Nanotechnol.*, 2019, **14**, 616–622.

5 S. V. Torti and F. M. Torti, *Nat. Nanotechnol.*, 2019, **14**, 499–500.
6 S. J. Dixon, K. M. Lemberg, M. R. Lamprecht, R. Skouta, E. M. Zaitsev, C. E. Gleason, D. N. Patel, A. J. Bauer, A. M. Cantley, W. S. Yang, B. Morrison 3rd and B. R. Stockwell, *Cell*, 2012, **149**, 1060–1072.
7 F. Zhang, F. Li, G. H. Lu, W. Nie, L. Zhang, Y. Lv, W. Bao, X. Gao, W. Wei, K. Pu and H. Y. Xie, *ACS Nano*, 2019, **13**, 5662–5673.
8 T. Liu, W. Liu, M. Zhang, W. Yu, F. Gao, C. Li, S. B. Wang, J. Feng and X. Z. Zhang, *ACS Nano*, 2018, **12**, 12181–12192.
9 D. W. Zheng, Q. Lei, J. Y. Zhu, J. X. Fan, C. X. Li, C. Li, Z. Xu, S. X. Cheng and X. Z. Zhang, *Nano Lett.*, 2017, **17**, 284–291.
10 S. Zanganeh, G. Hutter, R. Spitler, O. Lenkov, M. Mahmoudi, A. Shaw, J. S. Pajarinen, H. Nejadnik, S. Goodman, M. Moseley, L. M. Coussens and H. E. Daldrup-Link, *Nat. Nanotechnol.*, 2016, **11**, 986–994.
11 G. Chen, Y. Yang, Q. Xu, M. Ling, H. Lin, W. Ma, R. Sun, Y. Xu, X. Liu, N. Li, Z. Yu and M. Yu, *Nano Lett.*, 2020, **20**, 8141–8150.
12 Z. Tang, H. Zhang, Y. Liu, D. Ni, H. Zhang, J. Zhang, Z. Yao, M. He, J. Shi and W. Bu, *Adv. Mater.*, 2017, **29**, 1701683.
13 H. Liang, X. Wu, G. Zhao, K. Feng, K. Ni and X. Sun, *J. Am. Chem. Soc.*, 2021, **143**, 15812–15823.
14 H. Chen, X. Zeng, H. P. Tham, S. Z. F. Phua, W. Cheng, W. Zeng, H. Shi, L. Mei and Y. Zhao, *Angew. Chem., Int. Ed.*, 2019, **58**, 7641–7646.
15 Q. Wang, R. Dong, C. Wang, S. Xu, D. Chen, Y. Liang, B. Ren, W. Gao and Y. Cai, *ACS Appl. Mater. Interfaces*, 2019, **11**, 6201–6207.
16 S. Yu, T. Li, F. Ji, S. Zhao, K. Liu, Z. Zhang, W. Zhang and Y. Mei, *Mater. Today Adv.*, 2022, **14**, 100231.
17 T. Li, A. Zhang, G. Shao, M. Wei, B. Guo, G. Zhang, L. Li and W. Wang, *Adv. Funct. Mater.*, 2018, **28**, 1706066.
18 T. Li, S. Yu, B. Sun, Y. Li, X. Wang, Y. Pan, C. Song, Y. Ren, Z. Zhang, K. T. V. Grattan, Z. Wu and J. Zhao, *Sci. Adv.*, 2023, **9**, eadg4501.
19 W. Zhang, Y. Deng, J. Zhao, T. Zhang, X. Zhang, W. Song, L. Wang and T. Li, *Small*, 2023, e2207360, DOI: **10.1002/smll.202207360**.
20 H. Wang, S. Yu, J. Liao, X. Qing, D. Sun, F. Ji, W. Song, L. Wang and T. Li, *Front. Bioeng. Biotechnol.*, 2022, **10**, 903219.
21 H. Hu, C. Huang, M. Galluzzi, Q. Ye, R. Xiao, X. Yu and X. Du, *Research*, 2021, **2021**, DOI: **10.34133/2021/9786128**.
22 X. Du, H. Cui, Q. Zhao, J. Wang, H. Chen and Y. Wang, *Research*, 2019, **2019**, DOI: **10.34133/2019/6398296**.
23 H. Hu, M. Nie, M. Galluzzi, X. Yu and X. Du, *Adv. Funct. Mater.*, 2023, **33**, 2304634.
24 W. Wang, Z. Wu, L. Yang, T. Si and Q. He, *ACS Nano*, 2022, **16**, 9317–9328.
25 Z. Li, H. Zhang, Z. Wu and Q. He, *ChemNanoMat*, 2021, **7**, 1025–1029.
26 T. Xu, L.-P. Xu and X. Zhang, *Appl. Mater. Today*, 2017, **9**, 493–503.
27 F. Zhang, J. Zhuang, B. E. F. de Avila, S. Tang, Q. Zhang, R. H. Fang, L. Zhang and J. Wang, *ACS Nano*, 2019, **13**, 11996–12005.
28 B. Esteban-Fernandez de Avila, A. Martin, F. Soto, M. A. Lopez-Ramirez, S. Campuzano, G. M. Vasquez-Machado, W. Gao, L. Zhang and J. Wang, *ACS Nano*, 2015, **9**, 6756–6764.
29 G. Sheng, Y. Chen, L. Han, Y. Huang, X. Liu, L. Li and Z. Mao, *Acta Biomater.*, 2016, **43**, 251–261.
30 C. W. Hsu, M. H. Hsieh, M. C. Xiao, Y. H. Chou, T. H. Wang and W. H. Chiang, *Int. J. Biol. Macromol.*, 2020, **163**, 1106–1116.
31 C. Gao, P. Dong, Z. Lin, X. Guo, B. P. Jiang, S. Ji, H. Liang and X. C. Shen, *Chemistry*, 2018, **24**, 12827–12837.
32 Y. Long, X. Wu, Z. Li, J. Fan, X. Hu and B. Liu, *Biomater. Sci.*, 2020, **8**, 5088–5105.
33 P. Xue, R. Yang, L. Sun, Q. Li, L. Zhang, Z. Xu and Y. Kang, *Nano-Micro Lett.*, 2018, **10**, 74.
34 S. Ahmed, W. Wang, L. Bai, D. T. Gentekos, M. Hoyos and T. E. Mallouk, *ACS Nano*, 2016, **10**, 4763–4769.
35 M. Beltran-Gastelum, B. Esteban-Fernandez de Avila, H. Gong, P. L. Venugopalan, T. Hianik, J. Wang and V. Subjakova, *Chem. Phys. Chem.*, 2019, **20**, 3177–3180.
36 C. Zhang, W. Bu, D. Ni, S. Zhang, Q. Li, Z. Yao, J. Zhang, H. Yao, Z. Wang and J. Shi, *Angew. Chem., Int. Ed.*, 2016, **55**, 2101–2106.
37 X. Ai, Y. Wang, X. Hou, L. Yang, C. Zheng and L. Wu, *Analyst*, 2013, **138**, 3494–3501.
38 F. Wei, S. Kuang, T. W. Rees, X. Liao, J. Liu, D. Luo, J. Wang, X. Zhang, L. Ji and H. Chao, *Biomaterials*, 2021, **276**, 121064.
39 N. Wang, L. Zhu, D. Wang, M. Wang, Z. Lin and H. Tang, *Ultrason. Sonochem.*, 2010, **17**, 526–533.
40 S. Y. Li, H. Cheng, B. R. Xie, W. X. Qiu, L. L. Song, R. X. Zhuo and X. Z. Zhang, *Biomaterials*, 2016, **104**, 297–309.
41 X. Wang, J. Cai, L. Sun, S. Zhang, D. Gong, X. Li, S. Yue, L. Feng and D. Zhang, *ACS Appl. Mater. Interfaces*, 2019, **11**, 4745–4756.
42 D. Zhou, L. Ren, Y. C. Li, P. Xu, Y. Gao, G. Zhang, W. Wang, T. E. Mallouk and L. Li, *Chem. Commun.*, 2017, **53**, 11465–11468.